



1 Convective hydration in the tropical tropopause layer during the StratoClim aircraft campaign:
2 Pathway of an observed hydration patch

3
4 Keun-Ok Lee¹, Thibaut Dauhut¹, Jean-Pierre Chaboureau¹, Sergey Khaykin², Martina Krämer³ and
5 Christian Rolf³

6 ¹Laboratoire d'Aérodologie, Université de Toulouse, CNRS, UPS, Toulouse, France

7 ²LATMOS-IPSL, Université Versailles St-Quentin; Sorbonne Université, CNRS/INSU, Guyancourt, France

8 ³Institute for Energy and Climate Research – Stratosphere (IEK-7), Forschungszentrum Jülich, Jülich, Germany

9
10 ABSTRACT

11 The source and pathway of the hydration patch in the TTL (Tropical Tropopause Layer) that was measured
12 during the StratoClim field campaign during the Asian summer monsoon in 2017, and its connection to
13 convective overshoots are investigated. During flight #7, two remarkable layers are measured in the TTL
14 namely, (1) moist layer (ML) with water vapour content of 4.8–5.7 ppmv in altitudes of 18–19 km altitudes in
15 the lower stratosphere, and (2) ice layer (IL) with ice content up to 1.9 eq. ppmv in altitudes of 17–18 km in
16 the upper troposphere around 06:30 UTC on 8 August to the south of Kathmandu (Nepal). A Meso-NH
17 convection-permitting simulation succeeds in reproducing the characteristics of ML and IL. Through analysis,
18 we show that ML and IL are generated by convective overshoots that occurred over the Sichuan basin about
19 1.5 day before. Overshooting clouds develop up to 19 km, hydrating the lower stratosphere of up to 20 km
20 with 6401 t of water vapour by a strong-to-moderate mixing of the updraughts with the stratospheric air. A few
21 hours after the initial overshooting phase, a hydration patch is generated, and a large amount of water vapour
22 (above 18 ppmv) still remains at even higher altitudes up to 20.5 km ASL while the anvil cloud top descends
23 to 18.5 km. At the same time, a great part of the hydrometeors falls shortly, and the rest sublimates. Meanwhile
24 ice sediments out, the water vapour concentration in ML and IL decreases due to turbulent diffusion by mixing
25 with the tropospheric air. As the hydration patch continues to travel toward the south of Kathmandu,
26 tropospheric tracer concentration increases up to ~30 and 70 % in ML and IL, respectively. The air mass in the
27 layers becomes gradually diffused and it has less and less water vapour and ice content by mixing with the dry
28 tropospheric air.

29



30

31 **1. Introduction**

32 The Asian summer monsoon anticyclone is one of the most pronounced circulation patterns in the Northern
33 Hemisphere, and it is a dominant climatological feature of the global circulation during boreal summer (Mason
34 and Anderson, 1963; Randel and Park, 2006). The monsoon circulation horizontally covers large parts of
35 southern Asia and Middle East while it locates on the edge of the tropics and subtropics. It consists of cyclonic
36 flow and convergence in the lower troposphere together with strong anticyclonic circulation and divergence in
37 the upper troposphere. This circulation is coupled with persistent deep convection over the south Asia region
38 during summer (June to September) (Hoskins and Rodwell, 1995). The monsoon tropopause is relatively high;
39 the upper tropospheric anticyclonic circulation extends into the lower stratosphere spanning from around 300
40 hPa and 70 hPa, i.e. approximately the whole upper troposphere and lower stratosphere (UTLS) (Highwood
41 and Hoskins, 1998; Randel and Park, 2006).

42 Due to the strong dynamical signature in the UTLS, the influence of the monsoon is evident in chemical
43 constituents, i.e. water vapour is relatively high about 4.2 ppmv (Wright et al., 2011), ozone is relatively low
44 (Randel et al., 2001), and methane, nitrogen oxides, and carbon monoxide are relatively high (Park et al., 2004;
45 Li et al., 2005). Especially, the water vapour in the UTLS is controlled by the troposphere-to-stratosphere
46 transport of moisture across the tropical tropopause layer (TTL, located between ~150 hPa (355 K, 14 km) and
47 ~70 hPa (425 K, 18.5 km); Fueglistaler et al., 2009; Rolf et al., 2018). It is mainly driven by the large-scale
48 cold point tropopause temperature field, but also processes involving convection, gravity waves, and cirrus
49 cloud microphysics that modulate TTL humidity.

50 Convective overshoots that penetrate the tropopause directly inject air and water into the stratosphere.
51 Fundamentally, convection arises from the temperature difference between a parcel of warm air and the cooler
52 air surrounding it. Warm air, which is less dense, i.e. more buoyant, rises through the atmospheric column and
53 adiabatically expands and cools. When the temperature of the rising air parcel has cooled sufficiently, the water
54 vapour it contains will begin to condense and release latent heat. If air parcels within the convective core have
55 enough upward momentum, they continue to rise beyond their equilibrium level of zero buoyancy, and form
56 overshoots. The most energetic one forms an overshoot that penetrate into the lowermost stratosphere by
57 crossing the cold point tropopause. The convective overshoots have the potential to increase the humidity in
58 the stratosphere via rapid sublimation of convectively lofted ice and mixing with dry stratospheric air. This



59 has been demonstrated in previous studies in both modelling and measurement (Dessler and Sherwood, 2004;
60 Chaboureau et al., 2007; Jensen et al., 2007; Khaykin et al., 2016; Smith et al., 2017; Dauhut et al., 2018;
61 among others). Even a small volume of tropospheric air can carry a significant quantity of water in the
62 condensed phase. Mixing of tropospheric air with the surrounding stratosphere, which is typically sub-
63 saturated, facilitates the rapid sublimation of lofted ice. Also, the origin of the injected water to the TTL has
64 been studied by backward trajectory analysis at global scale, and it was found that the convective sources are
65 generally higher over the continental part of the Asian monsoon region in comparison to other tropical regions,
66 with shorter transit times (Tzella and Legras, 2005; Tissier and Legras, 2016). However, the net contribution
67 of convective overshoots to stratospheric water vapour concentration is not well understood at mesoscale and
68 is not well represented in global models because of the small spatial scales (less than a few kilometres) and
69 short time scales (less than few hours) over which convection occurs.

70 The tropical aircraft campaign of the Stratospheric and upper tropospheric processes for better Climate
71 predictions (StratoClim, www.stratoclim.org) took place in summer 2017. It aimed to improve our knowledge
72 of the key processes, i.e. microphysical, chemical and dynamical processes, which determine the composition
73 of the UTLS, such as the formation, loss, and redistribution of chemical constituents (water vapour, ozone, and
74 aerosol). During the campaign, eight dedicated flights were successfully operated with the objective of
75 documenting the connection between the moisture plumes in the UTLS and the convective sources from south
76 Kathmandu, Nepal, during summer monsoon season.

77 Our study focuses on part of flight #7 to the south of Kathmandu measuring the stratospheric hydration
78 in the altitudes between 17 and 19 km. The objective of our work is to investigate the source and pathway of
79 the localized moisture in the TTL that was measured by aircraft in connection to convective overshoot. This is
80 done using a combination of airborne and spaceborne observation as well as a convection-permitting
81 simulation performed with a fine resolution in the TTL.

82 A detailed description of the dataset is given in section 2. Section 3 presents the moistened TTL signature
83 captured by airborne and spaceborne observations and the numerical simulation. Section 4 demonstrates the
84 convective origin of the enhanced moisture and shows its evolution along its path in the lower stratosphere. A
85 summary and discussion of the findings of the present study are given in section 5.

86

87



88

89 **2. Data and method**

90 M55-Geophysica aircraft deployment in Kathmandu during Asian Summer Monsoon in July-August 2017
91 provided unprecedented sampling of the UTLS region above the southern slopes of Himalayas. More details
92 concerning the observational datasets used in this study together with the airborne and spaceborne
93 measurements and the convection-permitting simulation are provided in the following.

94

95 *2.1. StratoClim airborne observations*

96 During flight #7, the M55-Geophysica aircraft flew back and forth between Kathmandu in Nepal and west
97 Bengal in India (for the track, see the red line in Fig. 1) from 04:30 UTC to 06:50 UTC on 8 August 2017. In-
98 situ sensor onboard the aircraft measures the relative humidity with respect to ice (hereafter called simply
99 ‘relative humidity’ or ‘RH_{ice}’), temperature and wind speed and direction every 1 second. FLASH and FISH
100 instruments on board the Geophysica aircraft sampled the vertical water vapour and ice content distribution
101 every 1 second, respectively.

102 FLASH-A (Fluorescent Lyman-Alpha Stratospheric Hygrometer for Aircraft) is an advanced version of
103 the airborne FLASH instrument (Sitnikov et al, 2007; Khaykin et al., 2013) previously flown onboard the
104 M55-Geophysica aircraft. FLASH-A has a rear facing inlet allowing measurement of gas-phase water in the
105 altitude range between 12–21 km, with the latter being the aircraft ceiling altitude. Total uncertainty of water
106 vapour measurement amounts to 9 % with a detection limit of 0.2 ppmv, whereas the measurement precision
107 at 1 Hz sampling is better than 6 %.

108 FISH (Fast In situ Stratospheric Hygrometer) is a closed-path Lyman- α photo fragment fluorescence
109 hygrometer that measures total water (sum of gas phase and evaporated ice crystals) in the range of 1–1000
110 ppmv between 50 and 500 hPa levels with an accuracy and precision of 6–8 % and 0.3 ppmv (Zöger et al.,
111 1999; Meyer et al., 2015). The time resolution of the measurements is 1 Hz. Inside of ice clouds, ice water
112 content (IWC) is calculated by subtracting the gas phase water measured by FLASH from the total water
113 detected by FISH as described by Afchine et al. (2018). The minimum detectable IWC is 3×10^{-2} ppmv
114 ($\sim 3 \times 10^{-3}$ mg m⁻³).

115



116 2.2. Spaceborne observation

117 Calibrated thermal infrared brightness temperature (BT) data at 10.8 μm wavelength, acquired every 15 min
118 by the Spinning Enhanced Visible and Infrared Imager (SEVIRI) onboard the geostationary Meteosat Second
119 Generation satellite (MSG) were employed to investigate the evolution of deep convection. The spatial
120 resolution of the MSG-SEVIRI data used is 0.05° in both latitude and longitude. BT minima are generally
121 indicative of the cloud top overshoots associated with deep convection (e.g. Kato, 2006).

122 Vertical profiles of backscatter retrieved from the Cloud-Aerosol Lidar with Orthogonal Polarization
123 (CALIOP) on board CALIPSO (Winker et al. 2009) with a wavelength at 532 nm are used. CALIOP provides
124 observations of particles, including high clouds, with a very high sampling resolution, 30 and 335 m in the
125 vertical and horizontal directions, respectively.

126

127 2.3. Cloud-resolving numerical simulation

128 The target convective overshoots and the moistened TTL were simulated using the non-hydrostatic numerical
129 research model, Meso-NH (Lac et al. 2018). For a fine-scale analysis, the simulation uses about 400 million
130 grid points with horizontal grid spacing of 2.5 km. The vertical grid has 144 stretched levels (Gal-Chen and
131 Somerville, 1975) with a spacing of 250 m in the free troposphere and the stratosphere and a finer resolution
132 of 100 m close to the surface and between 16 and 19.5 km inside the TTL. The simulation domain covers
133 northern India and China (Fig. 1, $5000 \text{ km} \times 3600 \text{ km}$) encompassing the track of flight #7 and the overshooting
134 clouds over the Sichuan basin. The simulation was initialized at 00:00 UTC on 6 August 2017 and the initial
135 and lateral boundary conditions are provided by the operational European Centre for Medium-Range Weather
136 Forecasts (ECMWF) analyses every 6 hours. It ran for 3 days providing outputs every 1 hour.

137 The model employs a 1-moment bulk microphysical scheme (Pinty and Jabouille, 1998), which governs
138 the equations of six water categories (water vapour, cloud water, rainwater, pristine ice, snow and graupel).
139 For each particle type, the sizes follow a generalized Gamma distribution while power-law relationships allow
140 the mass and fall speed to be linked to the diameters. Except for cloud droplets, each condensed water species
141 has a nonzero fall speed. The turbulence parametrisation is based on a 1.5-order closure (Cuxart et al., 2000)
142 of the turbulent kinetic energy equation and uses the Bougeault and Lacarrere (1989) mixing length. The
143 transport scheme for momentum variables is the weighted essentially non-oscillatory (WENO) scheme (Shu
144 and Osher, 1988) while other variables are transported with the piecewise parabolic method (PPM) scheme



145 (Colella and Woodward, 1984).

146 To assess the simulation, airborne measurement data (along about 85.2°E, 25–26.5°N, blue line in Fig.
147 1) between 06:20 and 06:48 UTC on 8 August 2017 are compared to the simulation results averaged in a box
148 (85–85.5°E, 25–26.5°N, marked by ‘HYD’ in Fig. 1) at 06:00 UTC on the same day. The CALIOP backscatter
149 coefficients are compared to those simulated from the model outputs using the Meso-NH lidar simulator, which
150 takes into account all the predicted scattering particles (Chaboureau et al. 2011). The SEVIRI/MSG BTs are
151 compared to synthetic BTs computed offline using the Radiative Transfer for TIROS Operational Vertical
152 Sounder (RTTOV) code version 11.3 (Saunders et al. 2013) from the simulation outputs (Chaboureau et al.
153 2008).

154 In this study, a ‘hydration patch’ is defined as a region with a water vapour amount larger than the
155 background value at 410 K isentropic level. The background equals 5.2 ppmv which corresponds to the water
156 vapour averaged in the box 74–84°E, 15–25°N (shown with dashed line in Fig. 1). Such a hydration patch is
157 located within the moist layer (ML) of 18–19 km altitude (see Figure 2), corresponding to an enhanced value
158 of water vapour observed during the last descending of flight #7 (see section 3.1). Below the hydration patch,
159 the ice layer (IL) is located between 17 and 18 km, where an increase of ice content is observed during the
160 same period. The hydration patch is chased visually back in time every hour from 06:00 UTC on 8 August to
161 13:00 UTC on 6 August 2017, considering the prevailing wind direction and speed. The area of the hydration
162 patch is about 6,000 km², but it is reduced by one fourth to about 1,500 km² during the initial overshooting
163 phase in the convective region.

164 To understand the processes along the pathway of the hydration patch, four analysis times are selected:
165 1) a few hours before the overshoot development at 13:00 UTC on 6 August, 2) the overshoot development
166 time at 21:00 UTC on the same day, 3) a few hours after the overshoots at 12:00 UTC on 7 August, and 4) the
167 aircraft measurement time at 06:00 UTC on 8 August 2017. In this study, the overshoots are defined as
168 convective cloud tops that reach the lowermost stratosphere above 380 K level. A tracer of tropospheric air is
169 also calculated on line during the Meso-NH run. At the simulation initiation, the tropospheric and stratospheric
170 air masses are divided by a boundary at 380 K level, and the tracer values are set to 1 and 0 below and above,
171 respectively. In other words, pure concentration of tropospheric (stratospheric) air has tracer value equal to
172 100 (0) %.

173



174 **3. Convective hydration in the TTL**

175 *3.1. Moistened layers in the TTL*

176 FISH and FLASH instruments on board flight #7 measure moisture and ice content in the TTL to the south of
177 Kathmandu along the track of $\sim 85.2^\circ\text{E}$, $25\text{--}26.5^\circ\text{N}$ (blue line in Fig. 1) from 06:20 to 06:48 UTC on 8 August
178 2017. ML and IL were observed. ML is evident at altitudes of 18–19 km by the water vapour content of 4.8–5.7
179 ppmv (solid line in Fig. 2a), and IL is apparent at altitudes of 17–18 km with the ice content of up to 1.9 eq.
180 ppmv (solid line in Fig. 2b) and water vapour of 3.3–5.0 ppmv (solid line in Fig. 2a). The temperature
181 minimum, which defines the cold point tropopause (CPT, red line in Fig. 2c), equals -83.5°C at 17.8 km in
182 between ML and IL (black line in Fig. 2c). In ML, the potential temperature ranges between 394 and 428 K,
183 while in IL it ranges between 372 and 393 K (blue line in Fig. 2c). Figure 2d shows that RH_{ice} increases beyond
184 70 % in ML and IL, and that IL is partly super-saturated with RH_{ice} up to 118 %. In both ML and IL, strong
185 easterly wind prevails (black line in Fig. 2e) with wind speed exceeding 20 m s^{-1} (blue line in Fig. 2e), while
186 easterlies stronger than 30 m s^{-1} are seen at 17 and 18.5 km altitudes.

187 Figure 2 also evidences that Meso-NH succeeds in reproducing most of the measurements in the TTL.
188 It reproduces the enhanced amount of water vapour in both ML and IL. In ML, the simulated water vapour in
189 the range between 4.9–6.0 ppmv with an average value (black cross marks in Fig. 2a) of 5.5 ppmv reproduces
190 the measured 4.2–5.6 ppmv well. In IL, the appearance of ice (black cross marks in Fig. 2b) is simulated, but
191 with a maximum value of 0.65 eq. ppmv, a factor of 3 less compared to the measured concentrations. The
192 simulation captures well the CPT at 17.8 km altitude and -83.3°C (cross marks in Fig. 2c), RH_{ice} values of
193 70–100 % between 16.5–18.5-km altitudes (cross marks in Fig. 2d), and the strong easterly wind (black and
194 blue cross marks in Fig. 2e). Despite small vertical variations in water vapour and temperature that are missing
195 around the CPT, the simulation is good enough to being used to investigate the source and the pathways of
196 water in ML and IL.

197 A few hours before the Geophysica measurements and upstream, some clouds were observed in the TTL
198 by CALIOP around 20:00 UTC on 7 August 2017. Figure 3a shows a V-shaped region of strong backscatter
199 values of $0.001\text{--}0.008\text{ km}^{-1}\text{ sr}^{-1}$ from 15 to 18.5 km altitudes over India along the track of $25.5\text{--}31.5^\circ\text{N}$ (yellow
200 line in Fig. 1). The V-shaped strong backscatter region is successfully reproduced by Meso-NH (Fig. 3b) at
201 15–18.5-km altitudes between 26.5 and 31°N but with backscatter values lower than measured. The simulated
202 V-shaped region is characterized by low ice content (≥ 0.1 eq. ppmv, Fig. 3c) while an above-background



203 amount of water vapour of 5–7 ppmv is layered at altitudes higher than 18 km, (Fig. 3d), where ML is located.
204 The V-shaped strong backscatter region is possibly induced by waves propagating at these high altitudes, e.g.
205 gravity waves. Investigating the mechanism at its origin is however beyond the scope of this article. It is worth
206 noting that the above-background water vapour concentration and the ice content are already upstream
207 (93–95°E) about 10 hours before flight #7 (~85.2°E) and that Meso-NH is able to resolve clouds in the UTLS.
208

209 3.2. Target convective overshoots

210 In the region where ML and IL are located, the simulated hydration patch (water vapour ≥ 5.2 ppmv) is in
211 evidence at the 410 K level at 06:00 UTC on 8 August 2017 (Fig. 4a). It is positioned above high-level clouds,
212 as shown with BT values lower than -47°C in both the SEVIRI/MSG imagery and the Meso-NH simulation
213 in Fig. 5a and 5b (pointed by arrows), respectively. This hydration patch has been advected from the east by
214 the strong easterlies (about 25 m s^{-1} , see Fig. 2e). At 12:00 UTC on 7 August, it is located around eastern India
215 (Fig. 4c) and is associated with low BT values ($\leq -55^{\circ}\text{C}$) in both the MSG/SEVIRI imagery (pointed by an
216 arrow in Fig. 5c) and the Meso-NH simulation (Fig. 5d). This suggests that the hydration patch is generated
217 by the injection of water by convective overshoots. The convective overshoots start to be seen from 14:00 UTC
218 on 6 August over the Sichuan basin (Fig. 4e), and multiple overshoots develop in this region until 21:00 UTC.
219 During the period between 14:00 and 21:00 UTC, the developing overshoots collectively inject a large water
220 vapour amount of 6401 t above the CPT (as the result of integrating the water vapour content between the
221 convective overshoot altitude (17.8 km) and 22 km). The signature of overshoots is evidenced over the Sichuan
222 basin at 21:00 UTC by the large amount of water vapour in excess of 18 ppmv at 410 K level (Fig. 4d) and by
223 BT values lower than -80°C (Fig. 5e and 5f). At 13:00 UTC before the overshoot development, neither water
224 vapour mixing ratio larger than 5 ppmv nor BT values lower than -60°C are distinguishable over the Sichuan
225 basin (box in Fig. 5g and 5h).

226 In summary, a good agreement is achieved between the measurements (airborne and spaceborne) and
227 the Meso-NH simulation. The analysis of the simulation shows that the water-enhanced layers in ML and IL
228 observed to the south of Kathmandu around 06:30 UTC on 8 August were generated by the injection of water
229 by the convective overshoots produced over the Sichuan basin during 14:00–21:00 UTC on 6 August.

230

231



232 **4. Pathway of the hydration patch and processes affecting it**

233 *4.1. Evolution of the hydration patch during its way to the south of Kathmandu*

234 The hydration patch is described along its way from the Sichuan basin to the south of Kathmandu. In the
235 following, vertical sections of water vapour, ice content and tropospheric tracer are shown across the hydration
236 patch in the west-east orientation every 2 to 6 h (Figs. 6, 7, and 8). The vertical cross-sections are centred over
237 the hydration patch, all with the same size.

238

239 *4.1.1. Injection of water into the TTL by convective overshoots*

240 The vertical cross-sections of water vapour and ice content evidence that the large amounts of water vapour
241 and ice are injected above 380 K level by the convective overshoots that occurred during 15:00–21:00 UTC
242 on 6 August. At 13:00 UTC (Fig. 6a), just before the overshoot development, a strong upward motion is seen
243 at 16–18-km altitudes, while the cloud top (black solid line) is located in IL (about 17.5 km), just below the
244 CPT. At 15:00 UTC (Fig. 6b), a large amount of water vapour (≥ 15 ppmv) is in evidence in ML above 410 K
245 level while a large ice content in excess of 120 eq. ppmv is found in IL, between 380 and 410 K levels (Fig.
246 7b). Figure 8a–b shows that during 15:00–17:00 UTC the concentration of the tropospheric tracer increases in
247 both ML and IL with values of 0.04 and 0.3, respectively.

248 At 17:00 UTC even higher cloud top is apparent at ~ 19.5 km altitude (Fig. 6c), a large amount of water
249 vapour (≥ 18 ppmv) rises to ~ 20 km, around 103°E , and a large ice content (≥ 120 eq. ppmv) stays below 18
250 km altitude (Fig. 7c). It is worth noting the water injected by the convective overshoots at 15:00 UTC is still
251 apparent in ML at 17:00 UTC around 102°E with a water vapour mixing ratio above 9 ppmv (Fig. 6c). In a
252 similar way, the convectively-injected large moisture at 17:00 UTC around 103°E (Fig. 6c) is found in ML at
253 19:00 UTC around 102.5°E with a water vapour mixing ratio larger than 15 ppmv (Fig. 6d). At 19:00 UTC
254 (Fig. 6d), the strong convective updraughts perturb the isentropic surfaces (red solid lines), descending the 410
255 K level largely from about 18.5 to 17.5 km. At 21:00 UTC a higher cloud top is found above ML in a wide
256 area (102.3 – 103.3°E longitude). The injected water vapour (≥ 18 ppmv) is transported above 20.5 km (Fig. 6e)
257 while the concentration of 0.001–0.005 of the tropospheric tracer is seen in the water vapour pocket. The large
258 ice content exceeding 120 eq. ppmv is distributed mostly in IL (Fig. 7e). During 15:00–21:00 UTC (Fig. 8b–e),
259 a concentration of 0.02–0.2 of the tropospheric tracer is consistently seen in ML, while higher concentration
260 of 0.4 has been found in IL.



261

262 *4.1.2. Advection of the hydration patch along isentropes*

263 From 23:00 UTC on 6 August to 06:00 UTC on 8 August 2017, the convective overshoots gradually diminish
264 in the region of longitude $\sim 98\text{--}85^\circ\text{E}$ and latitude $\sim 28\text{--}25^\circ\text{N}$ (see Fig. 4). At 23:00 and 00:00 UTC, the anvil-
265 shaped cloud above 16 km altitude presents a rather flat cloud top around 19 km (Fig. 7f and 7g). The injected
266 large amount of water vapour ≥ 18 ppmv is evident in ML, even at higher altitudes up to 20.5 km (Fig. 6f and
267 6g) whereas the large ice content ≥ 120 eq. ppmv is no longer apparent in IL (Fig. 7f and 7g). During
268 06:00–18:00 UTC on 7 August, the water vapour mixing ratio in ML gradually decreases from 15 to ~ 9 ppmv,
269 meanwhile the air mass in IL becomes dry with a water vapour mixing ratio below 4 ppmv (Fig. 6h–j). During
270 the same period, the increase of tropospheric tracer concentration is evident in both ML and IL. The air mass
271 with concentration higher than 0.4 is apparent in IL while the air mass with a lower tropospheric concentration
272 around 0.02–0.3 is seen in IL (Fig. 8h–j).

273 The air mass with high tropospheric tracer concentration of 0.02–0.4 consistently exists in ML and IL
274 from 00:00 to 06:00 UTC on 8 August 2017 (Fig. 8k–l). During this period, the hydration patch is further
275 narrowed and widened in ML (Fig. 6k–l), and the air mass becomes drier in IL (≤ 3 ppmv). At 00:00 UTC
276 (Fig. 7k), new convection tops are apparent in altitudes of 16–17 km, and an increase of ice content above 3
277 eq. ppmv is seen in IL. Then a decrease of ice content down to 0.1–1 eq. ppmv distributes in IL at 06:00 UTC
278 where large ice content around 1–1.9 eq. ppmv was measured (see Fig. 2b).

279

280 *4.2. Processes affecting the hydration patch*

281 The processes that affect the moist and ice layers are further described. To this objective, average quantities
282 are calculated in ML and IL. The hourly evolution of water vapour, ice content, temperature, and RH_{ice} shows
283 the lifetime of the injected water in ML and IL along the pathway of the hydration patch (Fig. 9). The profiles
284 of tropospheric tracer, temperature, RH_{ice} , water vapour, ice content and wind speed give a vertical view in the
285 column across the tropical tropopause layer (Fig. 10). A scatter plot using tropospheric tracer and water vapour
286 highlights the mixing processes occurring in the hydration patch (Fig. 11).

287

288 *4.2.1. Mixing of the overshoots with the stratospheric air*

289 The hourly evolution of the average water vapour and the ice content along the pathway of the hydrated layer



290 demonstrates the hydration in the TTL by the convective overshoots (Figs. 6 and 7). During the development
291 of the convective overshoots between 14:00 and 21:00 UTC on 6 August 2017, the average water vapour
292 mixing ratio increases to 5.7 ppmv in IL (yellow solid line, Fig. 9a), while a large mixing ratio of 6.5 ppmv is
293 seen in ML (blue solid line in Fig. 9a). The ice content reaches more than 200 eq. ppmv in both layers even
294 more than 300 eq. ppmv in IL (Fig. 9b). Until 17:00 UTC, the temperature increases in both layers (solid lines
295 in Fig. 9c), indicating the mixing with the warmer stratospheric air. Because of this entrained stratospheric air,
296 RH_{ice} decreases largely below 60 % in ML (blue line with symbols in Fig. 9c), and down to 90 % in IL (yellow
297 line with symbols). The active mixing of the convective overshoots with the stratospheric air between 14:00
298 and 21:00 UTC is also evidenced by the evolution of vertical profiles of tropospheric tracer (Fig. 10a). The
299 tropospheric tracer concentration increases from 0 to 5 % in ML (yellow to green lines in Fig. 10a), while the
300 stratospheric air concentration (1 minus tracer) increases of ~ 5 % in IL. The temperature increases in both ML
301 and IL (yellow to green lines in Fig. 10b) where the relative humidity decreases (yellow to green lines in Fig.
302 10c).

303 The scatter plot of the tropospheric tracer and water vapour mixing ratio (Fig. 11) evidences the large
304 mixing of tropospheric and stratospheric air masses in the TTL (14–22 km altitudes). A large evolution of the
305 tropospheric tracer–water vapour diagram is found from 13:00 to 21:00 UTC on 6 August (Fig. 11a and 11b).
306 At 13:00 UTC before the development of the convective overshoots, the air mass with potential temperature
307 (θ) of 410–420 K (yellow dots), corresponding to ML, is relatively dry with a water vapour mixing ratio of
308 5–7.2 ppmv (Fig. 11a) and very small compounds of stratospheric air (tracer ≤ 0.1 %). The air mass with θ of
309 380–390 K (black dots), corresponding to IL, has a low water vapour mixing ratio of 3–7.5 ppmv. At 21:00
310 UTC (Fig. 11b), the air mass with θ between 410 and 420 K becomes very humid (5.5–13.6 ppmv of water
311 vapour) and the concentration of tropospheric tracer increases to 0.2–8 %. Moreover the air mass with very-
312 high θ of 450–460 K (purple dots) is moistened largely as shown by a water vapour mixing ratio above 15
313 ppmv. So does the air mass with θ between 390 and 410 K, which is both moistened and enriched by the
314 tropospheric tracer with a concentration of 5–60 % (red to orange dots, Fig. 11b). The convective overshoots
315 also impact the air mass below the CPT by widening the range of the water vapour mixing ratio with θ between
316 370 and 380 K (grey dots in Fig. 11a and b) from 3.2–13.9 ppmv at 13:00 UTC (Fig. 11a) to 0–18.8 ppmv at
317 21:00 UTC (Fig. 11b).

318 From 17:00 UTC on 6 August to 02:00 UTC on 7 August, Fig. 9c shows that the temperature decreases



319 gradually (solid lines), while the relative humidity increases (lines with symbols). In ML and IL, a great part
320 of ice contents, especially snow and graupel fall quickly (dashed line in Fig. 9b), and the rest sublimates.
321 Meanwhile ice sediment out, the water vapour concentration slightly decreases due to mixing (blue solid line
322 in Fig. 9a). In ML, the relative humidity increases (in range of 65–80 %) mainly due to the temperature
323 decrease (in range of -78 and -82°C) (solid lines, Fig. 9c). During this period, the easterly wind is nearly
324 constant with the relatively-weak speed of $\sim 15\text{ m s}^{-1}$ in ML and $\sim 16.5\text{ m s}^{-1}$ in IL (yellow to green lines, Fig.
325 10f). After 7 August, in ML, the relative humidity less than 80 % indicates strong sub-saturation where a very
326 small amount (0.1–0.3 eq. ppmv) of cloud ice still resides. This probably induced by the domain-averaged
327 analysis.

328

329 *4.2.2. Turbulent mixing of the hydration patch with the tropospheric air*

330 After the development of the convective overshoots, the hydration patch travels westward across India and
331 north Bangladesh from 21:00 UTC on 6 August to 06:00 UTC on 8 August (Fig. 4). During its travel, the air
332 mass in ML and IL has less and less amount of water vapour and ice content (Fig. 9a–b).

333 Between 21:00 UTC on 6 August and 12:00 UTC on 7 August, the concentration of tropospheric tracer
334 increases at high altitudes with θ between 410 and 420 K up to 18 % (yellow dots, Fig. 11b–c). At the same
335 time, the water vapour decreases by a factor of two, in the range of 5–9.6 ppmv. This can be also seen in the
336 vertical profiles for which the concentration of tropospheric tracer increases at 12:00 UTC on 7 August in both
337 ML and IL (green to blue lines, Fig. 10a) and the water vapour decreases (green to blue lines, Fig. 10d). The
338 two layers become colder by $\sim 3^{\circ}\text{C}$ (green to blue lines in Fig. 10b). In IL (Fig. 9c), RH_{ice} oscillates mostly
339 driven by temperature variation. Over time, the air mass in ML and IL gets colder and less humid by the
340 lowered cloud top below 17 km altitude. In both ML and IL, the easterly winds weaken below 15 m s^{-1} .
341 Moreover, the turbulent kinetic energy (TKE) increases from 0.1–0.3 $\text{m}^2\text{ s}^{-2}$ at 21:00 UTC to 0.2–0.7 $\text{m}^2\text{ s}^{-2}$ at
342 12:00 UTC in ML and IL (data not shown). These results suggest that the water vapour concentration in ML
343 and IL decreases due to the turbulent diffusion in both the vertical and the horizontal direction consistent with
344 the increase of tropospheric tracer. The rapid decrease of ice content in IL due to both sublimation and
345 sedimentation (Fig. 7f–i) results in the lowering of the cloud top from 17 to below 16 km at $97\text{--}101^{\circ}\text{E}$ at 06:00
346 UTC (Fig. 7h), and finally to 15 km around 95.5°E at 12:00 UTC (Fig. 7i).

347 Further increased tropospheric tracer concentration is distinguished from 12:00 UTC on 7 August to



348 06:00 UTC on 8 August 2017 in ML and IL (blue to red lines, Fig. 10a). Moreover the tropospheric tracer
349 concentration reaches to about 30 and 70 % in ML and IL, respectively while the water vapour decreases (Fig.
350 10a and 11d). During this time, the cloud top height of convective cloud descends below 14 km (Fig. 6i–l),
351 where RH_{ice} dramatically decreases (Figs. 2d, 10c). The entrained cold tropospheric air and the hydrostatic
352 adjustment decrease the temperature in ML and IL (Fig. 10b). It is worth noting the shape of the temperature
353 profile that becomes straight upward in the altitudes of 17–18.5 km during the overshoot activity (green line,
354 Fig. 10b). Also it is worth noting the decrease of ice content less than 0.3 eq. ppmv (blue to red line, Fig. 10e),
355 and the large-decrease of relative humidity in altitudes below 17.5 km.

356 The increased tropospheric tracer concentration in ML and IL is as well seen by the tracer–vapour
357 diagram of Fig. 11c–d. The concentration of tropospheric tracer increases at high altitudes with θ between 410
358 and 420 K (yellow dots) up to 20 % at 06:00 UTC on 8 August 2017, meanwhile the tropospheric air
359 concentration increases up to 50 % at the altitudes with θ between 390 and 400 K (red dots in Fig. 11d). During
360 the period (12:00 UTC on 7 August to 06:00 UTC on 8 August), the water vapour decreases in all altitudes
361 with θ above 380 K (Fig. 11c–d). It decreases from ~ 9.6 below 6.2 ppmv in ML (θ between 410–430 K, yellow
362 and green dots) while dropping below 5 ppmv in IL (θ between 380–400 K, red and black dots). The reduced
363 ice content in ML and IL might be induced by sublimation thanks to the mixing with the dry tropospheric air
364 ($RH_{ice} \sim 50\text{--}70\%$) of below 16 km level (red line in Fig. 10c and cross marks in Fig. 2d). The air mixing of
365 tropospheric and stratospheric air masses might be induced by the vertical wind shear with the maxima wind
366 speeds in exceed of 30 m s^{-1} at ~ 17 and 18.5 km altitudes (see Fig. 2e, average value in range of 18 and 25 m
367 s^{-1} of red line in Fig. 10f). With the strengthened easterlies, the air mass in IL is well mixed rather than
368 conserved in this layer. Also, this wind shear layer locates below and above the CPT (Fig. 2c, 2e), thus it results
369 in the strait upward temperature profile at 06:00 UTC on 8 August as seen in Fig. 10b (red line). The air mass
370 in ML and IL has large TKE values of $0.5\text{ m}^2\text{ s}^{-2}$ (not shown).

371

372 5. Conclusions

373 The source and pathways of the hydration patch in the TTL (Tropical Tropopause Layer) that was measured
374 during flight #7 of the StratoClim 2017 field campaign during the Asian summer monsoon, and its connection
375 to convective overshoot are investigated. During the Geophysica flight #7 around 06:30 UTC on 8 August
376 2017, two remarkable layers were observed to the south of Kathmandu above and below the CPT located at



377 17.8 km, a moist layer (ML) with large water vapour content of 4.2–5.6 ppmv in altitudes of 18–19 km in the
378 lower stratosphere, and an ice layer (IL) with large ice content up to 1.9 eq. ppmv at altitudes of 17–18 km in
379 the upper troposphere. The Meso-NH numerical simulation run with a 2.5 km horizontal grid spacing succeeds
380 in reproducing ML and IL. Through analysis using airborne and spaceborne measurements and the numerical
381 simulation, we show that the measured hydration patch in ML found in the south of Kathmandu (~85°E) was
382 produced by the convective overshoots that occurred over the Sichuan basin (~103°E) between 14:00 and
383 21:00 UTC on 6 August 2017. The key hydration processes are summarized schematically in Fig. 12.

384 The convective overshoots develop up to 19.5 km altitude in the Sichuan basin, and transport large
385 amount of water vapour of 6.5 ppmv to ML and ice content in excess of 300 eq. ppmv to IL. Between 15:00
386 and 21:00 UTC, multiple overshooting clouds collectively hydrate the lower stratosphere resulting in the total
387 amount of water vapour of 6401 t. It is also worth noting the large concentration of water vapour of over 18
388 ppmv up to 20 km level which is above the convective cloud top of 19.5 km (a yellow ellipsoid in Fig. 12a).
389 This feature is similarly seen during the development of the Hector the Convective in the Tiwi Islands (Dauhut
390 et al., 2018), however, the magnitude is ~10 ppmv higher in the present event. The concentration of the
391 tropospheric tracer reaches to 8 and ~60 % in ML and IL, respectively, indicating the strong mixing of the
392 convective updraughts with the stratospheric air (black arrows in Fig. 12a). The strong convective updraughts
393 perturb the isentropic surfaces (red line in Fig. 12a), descending the 410 K level from 18.5 to 17.5 km. During
394 these convective events, the mixing of the tropospheric and stratospheric air masses increases the temperature
395 in ML and IL. Moreover, the moderate -not intense- easterly wind (~15 m s⁻¹) prevails constantly in these
396 levels, and it does not interrupt the convection developing vigorously in altitude (19.5 km ASL) and reaching
397 the lower stratosphere.

398 The injected water by the convective overshoots generates the hydration patch, i.e. large water vapour
399 in ML (ellipse in Fig. 12b). During its westward travel, its altitude is kept constant by the moderate easterlies
400 of about 15 m s⁻¹ in ML and IL. The tropospheric tracer concentration is continuously increased in these layers,
401 where the above-background amount of water vapour is still remained and where the ice content gradually
402 sediments out and forms again along the pathway. It is highlighted that the large transported amount of water
403 vapour (≥18 ppmv) still remains at high altitudes of up to 20.5 km even when the anvil cloud top descends to
404 18.5 km. Later on, the cloud top is still seen around 16–17 km level, keeping the large RH_{ice} (about 95 %) in
405 these altitudes. A part of the water vapour has been lost due to ice formation and sedimentation and the



406 turbulent diffusion in both vertical and the horizontal direction (black arrows in Fig. 12b). Thanks to the
407 turbulent mixing with colder tropospheric air mass, the remaining large amounts of water vapour in ML and
408 IL are partly deposited, and then ice falls rapidly below the ice layer. This falling of ice and a reduced updraught
409 are evident by the lowered cloud top height partly from 17 to ~15 km (Fig. 12c).

410 Then the hydration patch continues to travel to the south of Kathmandu, with even higher tropospheric
411 tracer concentration of ~30 and 70 % in ML and IL, respectively (darkened blue shades in Fig. 12c). During
412 the same period, the top of convective clouds further descends below 14 km, thus the layer below IL, i.e. 15–17
413 km, becomes dry with RH_{ice} below 70 %. Due to mixing with the dry tropospheric air, the remaining ice content
414 in IL gradually sublimates (hatched area in Fig. 12c), and the remaining water vapour in ML gradually diffused
415 in horizontal and vertical direction (ellipse). It is also true that the ice content in IL is locally influenced by
416 new convection with cloud top in altitudes 16–17 km about 6 h before flight #7. The continuous air mixing
417 might be induced by the vertical wind shear in altitudes 15–19 km where the wind speed varies from ~18 to
418 25 m s^{-1} (red bold arrows in Fig. 12c). The vertical mixing due to wind shear modifies the temperature profile
419 to the straight-upward in 17–18 km rather than bending. Also, vertical motions caused by gravity waves
420 breaking might play an important role in the transport of tropospheric air into the TTL. In addition, the
421 horizontal divergence that is remained in the lower stratosphere after the overshoots descending might let the
422 tropospheric air continues to ascend.

423 Many of previous Lagrangian studies (e.g. Tzella and Legras, 2011; Tissier and Legras, 2016)
424 demonstrated the link between the moistened TTL and remote overshoots using large-scale numerical
425 simulations. Thanks to the combination of aircraft measurement and a 3-day convection-permitting simulation,
426 this study shed light on the processes along the pathway of a hydration patch from overshooting clouds for 1.5
427 days, showing the 3-D evolution of water vapour and ice content.

428 This study focuses on the hydration patch that was measured during the last descending of flight #7 and
429 the corresponding convective overshoots over the Sichuan basin. Here, the average water vapour amount in
430 the lower stratosphere is 6.5 ppmv during the convective event while a water vapour of 6 ppmv is found above
431 West Africa during the monsoon season by Khaykin et al. (2009). By comparison, convection developing
432 during the Asian monsoon over the Sichuan basin had a similar impact on the stratospheric water budget as
433 above West Africa. From the estimated value of 6401 t, we can also confirm that the local impact of overshoots
434 developed during the Asian summer monsoon is stronger than the one over tropical Africa (300–500 t



435 according to Liu et al., 2010) and Hector the Convectoid over the Tiwi Islands (2776 t according to Dauhut et
436 al., 2015). Because of a large variety in the lifetime and horizontal scale of overshoots, an accumulation of
437 more event-scale analyses is important. To understand how much water vapour and ice are generally injected
438 into the TTL through convective overshoots during the Asian summer monsoon is currently investigated in a
439 follow-up study. Further, it would be interesting to investigate the transport of chemical constituents, e.g.
440 methane, nitrogen oxides, and carbon monoxide, via convective overshoots during this season.

441

442 **Author contribution**

443 KOL, TD and JPC designed the numerical simulation, and JPC performed the simulation. KOL, TD and JPC
444 designed the manuscript and analyses. SK provided the FLASH instrument data, and MK and CR provided
445 the FISH instrument data. KOL prepared the manuscript with contributions from all co-authors.

446

447 **Acknowledgement**

448 This study is funded by the StratoClim project by the European Union Seventh Framework Programme under
449 grant agreement no 603557 and the IDEX TEASAO project. Computer resources were allocated by GENCI
450 through project 90569.

451

452 **References**

453 Afchine, A., Rolf, C., Costa, A., Spelten, N., Riese, M., Buchholz, B., Ebert, V., Heller, R., Kaufmann, S.,
454 Minikin, A., Voigt, C., Zöger, M., Smith, J., Lawson, P., Lykov, A., Khaykin, S., and Krämer, M.: Ice
455 particle sampling from aircraft – influence of the probing position on the ice water content, Atmos.
456 Meas. Tech., 11, 4015-4031, <https://doi.org/10.5194/amt-11-4015-2018>, 2018.

457 Bougeault, P. and Lacarrère, P.: Parameterization of orography-induced turbulence in a meso-beta-scale model.
458 Mon. Weather Rev. 117(8): 1872–1890, 1989.

459 Chaboureaud, J.-P., Cammas, J.-P., Duron, J., Mascart, P. J., Sitnikov, N. M., and Voessing, H. J.: A numerical
460 study of tropical cross-tropopause transport by convective overshoots, Atmos. Chem. Phys., 7, 1731–
461 1740, 2007.

462 Chaboureaud, J.-P., and Coauthors: A midlatitude precipitating cloud database validated with satellite
463 observations. J. Appl. Meteor. Climatol., 47, 1337–1353, doi.org/10.1175/2007JAMC1731.1, 2008.



- 464 Chaboureau, J.-P., and Coauthors: Long-range transport of Saharan dust and its radiative impact on
465 precipitation forecast: A case study during the Convective and Orographically-induced Precipitation
466 Study (COPS). *Quart. J. Roy. Meteor. Soc.*, 137, 236–251, doi.org/10.1002/qj.719, 2011.
- 467 Colella, P. and Woodward, P. R.: The piecewise parabolic method (PPM) for gas dynamical simulations. *J.*
468 *Comput. Phys.* 54: 174–201, doi:10.1016/0021-9991(84)90143-8, 1984.
- 469 Cuxart, J., Bougeault, P., and Redelsperger, J. L.: A turbulence scheme allowing for mesoscale and large-eddy
470 simulations. *Q. J. R. Meteorol. Soc.* 126(562): 1–30, doi: 10.1002/qj.49712656202, 2000.
- 471 Dauhut, T., Chaboureau, J. P., Escobar, J., and Mascart, P.: Large-eddy simulations of hector the convector
472 making the stratosphere wetter. *Atmos. Sci. Let.* 16, 135–140, doi:10.1002/asl2.534. 2015.
- 473 Dauhut, T., Chaboureau, J. P., Haynes, P. H., and Lane, T. P.: The mechanisms leading to a stratospheric
474 hydration by overshooting convection. Accepted to *J. Atmos. Sci.*, 2018.
- 475 Dessler, A. E. and Sherwood, S. C.: Effect of convection on the summertime extratropical lower stratosphere,
476 *J. Geophys. Res.*, 109, D23301, doi:10.1029/2004JD005209, 2004.
- 477 Fueglistaler, S., Dessler, A. E., Dunkerton, T. J., Folkins, I., Fu, Q., and Mote, P. W.: Tropical tropopause layer,
478 *Rev. Geophys.*, 47, RG1004, doi:10.1029/2008RG000267, 2009.
- 479 Gal-Chen, T. and Somerville, R. C. J.: On the use of a coordinate transformation for the solution of the Navier-
480 Stokes equations. *J. Comput. Phys.* 17: 209–228, doi:10.1016/0021-9991(75)90037-6, 1975.
- 481 Highwood, E. J., and Hoskins, B. J.: The tropical tropopause, *Q. J. R. Meteorol. Soc.*, 124, 1579–1604, 1998.
- 482 Hoskins, B. J. and Rodwell, M. J.: A model of the Asian summer monsoon, I, The global scale, *J. Atmos. Sci.*,
483 52, 1329–1340, 1995.
- 484 Jensen, E., Ackerman, A. S. and Smith, J. A.: Can overshooting convection dehydrate the tropical tropopause
485 layer? *J. Geophys. Res.*, 112, D11209, doi:10.1029/2006JD007943, 2007.
- 486 Kato T.: Structure of the band-shaped precipitation system inducing the heavy rainfall observed over
487 northern Kyushu, Japan on 29 June 1999. *J. Meteor. Soc. Japan.* 84, 129–153, 2006.
- 488 Khaykin, S. M., Pommereau, J.-P., Riviere, E. D., Held, G., Ploeger, F., Gysels, M., Amarouches, N., Vernier,
489 J.-P., Wienhold, F. G., and Ionov, D.: Evidence of horizontal and vertical transport of water in the
490 southern hemisphere tropical tropopause layer (TTL) from high-resolution balloon observation, *Atmos.*
491 *Chem. Phys.*, 16, 12273–12286, 2016.
- 492 Khaykin, S., Pommereau, J.-P., Korshunov, L., Yushkov, V., Nielsen, J., Larsen, N., Christense, T., Garnier, A.,



- 493 Lukyanov, A., and Williams, E.: Hydration of the lower stratosphere by ice crystal geysers over land
494 convective systems, 9, 2275–2287, 2009.
- 495 Khaykin, S. M., Engel, I., Vömel, H., Formanyuk, I. M., Kivi, R., Korshunov, L. I., Krämer, M., Lykov, A. D.,
496 Meier, S., Naebert, T., Pitts, M. C., Santee, M. L., Spelten, N., Wienhold, F. G., Yushkov, V. A., and
497 Peter, T.: Arctic stratospheric dehydration – Part I: Unprecedented observation of vertical redistribution
498 of water, Atmos. Chem. Phys., 13, 11503–11517, <https://doi.org/10.5194/acp-13-11503-2013>, 2013.
- 499 Lac, C., Chaboureau, J. P., Masson, V., Pinty, J. P., Tulet, P., Escobar, J., Leriche, M., Barthe, C., Aouizerats,
500 B., Augros, C., Aumond, P., Auguste, F., Bechtold, P., Berthet, S., Bieilli, S., Bosseur, F., Caumont, O.,
501 Cohard, J. M., Colin, J., Couvreur, F., Cuxart, J., Delautier, J., Dauhut, T., Ducrocq, V., Filippi, J.B.,
502 Gazen, D., Geoffroy, O., Gheusi, F., Honnert, R., Lafore, J. P., Lebeaupin, Brossier C., Libois, Q., Lunet,
503 T., Mari, C., Maric, T., Mascart, P., Mogé, M., Molinié, G., Nuissier, O., Pantillon, F., Peyrillé, P.,
504 Pergaud, J., Perraud, E., Pianezze, J., Redelsperger, J. L., Ricard, D., Richard, E., Riette, S., Rodier, Q.,
505 Schoetter, R., Seyfried, L., Stein, J., Suhre, K., Taufour, M., Thouron, O., Turner, S., Verrelle, S., Vié,
506 B., Visentin, F., Vionnet, V., and Wautelet, P.: Overview of the Meso-NH model version 5.4 and its
507 applications. Geosci. Model Dev., 11, 1929–1969, 2018.
- 508 Liu, C., and Zipser, E. J.: Global distribution of convection penetrating the tropical tropopause, J. Geophys.
509 Res., 110, D23104, doi:10.1029/2005JD006063, 2005.
- 510 Masson, V., Le Moigne, P., Martin, E., Faroux, S., Alias, A., Alkama, R., Belamari, S., Bardu, A., Boone, A.,
511 Bouysse, F., Brousseau, P., Brun, E., Calvet, J.C., Carrer, D., Decharme, B., Delire, C., Donier, S.,
512 Essaouini, K., Gibelin, A. L., Giordani, H., Habets, F., Jidane, M., Kerdraon, G., Kourzeneva, E.,
513 Lafaysse, M., Lafont, S., Lebeaupin, B.C., Lemonsu, A., Mahfouf, J.F., Marguinaud, P., Mokhtari, M.,
514 Morin, S., Pigeon, G., Salgado, R., Seity, Y., Taillefer, F., Tanguy, G., Tulet, P., Vincendon, B., Vionnet,
515 V., and Voldoire, A.: The surfex v7.2 land and ocean surface platform for coupled or offline simulation
516 of earth surface variables and fluxes. Geosci. Model Dev. 6(4): 929–960, doi:10.5194/gmd-6-929-2013,
517 2013.
- 518 Mason, R. and Anderson, C.: The development and decay of the 100-MB. Summertime anticyclone over
519 southern Asia. Mon. Wea. Rev., 1, 3–12, 1963.
- 520 Meyer, J., Rolf, C., Schiller, C., Rohs, S., Spelten, N., Afchine, A., Zöger, M., Sitnikov, N., Thornberry, T. D.,
521 Rollins, A. W., Bozóki, Z., Tátrai, D., Ebert, V., Kühnreich, B., Mackrodt, P., Möhler, O., Saathoff, H.,



- 522 Rosenlof, K. H., and Krämer, M.: Two decades of water vapor measurements with the FISH fluorescence
523 hygrometer: a review, Atmos. Chem. Phys., 15, 8521–8538, <https://doi.org/10.5194/acp-15-8521-2015>,
524 2015.
- 525 Park, M., Randel, W. J., Kinnison, E. J., Garcia, R. R., and Choi, W.: Seasonal variation of methane, water
526 vapor and nitrogen oxides near the tropopause: Satellite observations and model simulation, J. Geophys.
527 Res., 109, D03302, doi:10.1029/2003JD003706, 2004.
- 528 Pinty, J. P. and Jabouille, P.: A mixed-phased cloud parametrization for use in a mesoscale non-hydrostatic
529 model: Simulations of a squall line and of orographic precipitation. In: Proc. Of the Conference on Cloud
530 Physics. Amer. Meteorol. Soc, Boston: Everett, WA, USA, 17–21 Aug. 1998. Pp. 217–220, 1998.
- 531 Randel, W. J. and Park, M.: Deep convective influence on the Asian summer monsoon anticyclone and
532 associated tracer variability observed with Atmospheric Infrared Sounder (AIRS), J. Geophys. Res., 111,
533 D12314, doi:10.1029/2005JD006490, 2006.
- 534 Randel, W. J., Wu, F., Gettelman, A., Russell, J. M., Zawodny, J. M., and Oltmans, S. J.: Seasonal variation of
535 water vapour in the lower stratosphere observed in Halogen Occultation Experiment data, J. Geophys.
536 Res., 106(D13), 14313–14325, 2001.
- 537 Rolf, C., Vogel, B., Hoor, P., Afchine, A., Günther, G., Krämer, M., Müller, R., Müller, S., Spelten, N., and
538 Riese, M.: Water vapor increase in the lower stratosphere of the northern hemisphere due to the Asian
539 monsoon anticyclone observed during the TACTS/ESMVal campaigns, Atmos. Chem. Phys., 18,
540 2973–2983, <http://doi.org/10.5194/acp-18-2973-2018>, 2018.
- 541 Saunders, R., Hocking, J., Rundle, D., Rayer, P., Matricardi, M., Geer, A., Lupu, C., Brunel, P., and Vidot, J.:
542 RTTOV-11—Science and validation report. NWP SAF Tech. Rep., 62 pp.,
543 https://www.nwpsaf.eu/site/download/documentation/rtm/docs_rtov11/rtov11_svr.pdf. 2013.
- 544 Shu, C. W. and Osher, S.: Efficient implementation of essentially non-oscillatory shock-capturing schemes.
545 Journal of Computational Physics 77(2): 439–471, 1988.
- 546 Sitnikov, N. M., Yushkov, V. A., Afchine, A. A., Korshunov, L. I., Astakhov, V. I., Elanovskii, A. E., Kraemer,
547 M., Mangold, A., Schiller, C., and Ravegnani, F.: The FLASH instrument for water vapor measurements
548 on board the high-altitude airplane. Instrum. Exp. Tech., 50, 113–121, 2007.
- 549 Smith, J. B., Wilmouth, D. M., Bedka, K. M., Bowman, K. P., Homeyer, C. R., Dykema, J. A., Sargent, M. R.,
550 Clapp, C. E., Leroy, S. S., Sayres, D. S., Dean-Day, J. M., Bui, T. P., and Anderson, J. G.: A case study



551 of convectively sourced water vapor observed in the overworld stratosphere over the United States. J.
552 Geophys. Res., 122, 9529–9554, doi:10.1002/2017JD026831, 2017.

553 Tissier, A.-S. and Legras, B.: Convective sources of trajectories traversing the tropical tropopause layer. Atmos.
554 Chem. Phys., 16, 3383–3398, 2016.

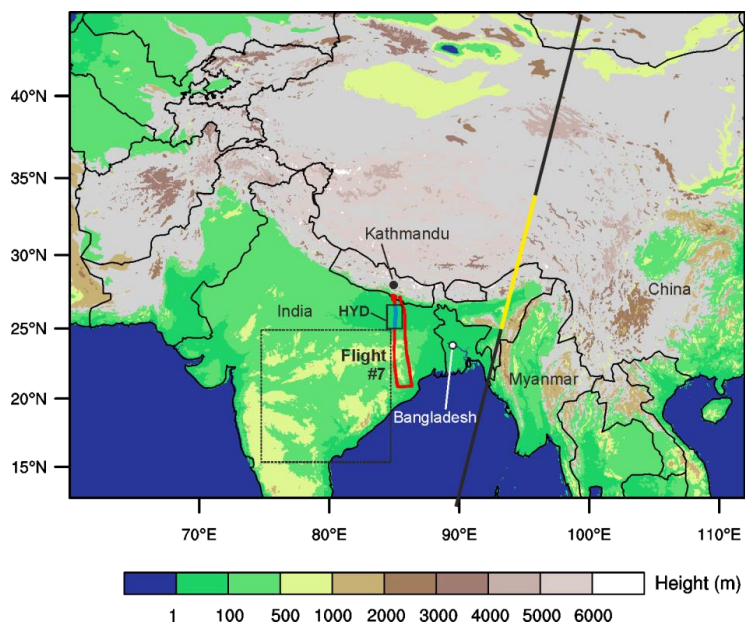
555 Tzella, A. and Legras, B.: A Lagrangian particle dispersion model FLEXPART version 6.2. Atmos. Chem.
556 Phys., 5, 2461–2474, doi:10.5194/acp-5-2461-2005, 2005.

557 Winker, D. M., Vaughan, M. A., Omar, A., Hu, Y., Powell, K. A., Liu, Z., Hunt, W. H., and Young, S. A.:
558 Overview of the CALIPSO mission and CALIOP data processing algorithms. J. Atmos. Oceanic
559 Technol., 26, 2310–2323, doi:10.1175/2009JTECHA1281.1, 2009.

560 Wright, J. S., Fu, R., Fueglistaler, S., Liu, Y. S., and Zhang, Y.: The influence of summertime convection over
561 Southeast Asia on water vapor in the tropical stratosphere. J. Geophys. Res., 116, D12302,
562 doi:10.1029/2010JD015416, 2011.

563 Zöger, M., Afchine, A., Eicke, N., Gerhards, M.-T., Klein, E., McKenna, D., Mörschel, U., Schmidt, U., Tan,
564 V., Tuitjer, F., Woyke, T., and Schiller, C.: Fast in situ stratospheric hygrometers: A new family of
565 balloon-borne and airborne Lyman-photofragment fluorescence hygrometers, J. Geophys. Res., 104,
566 1807–1816, 1999.

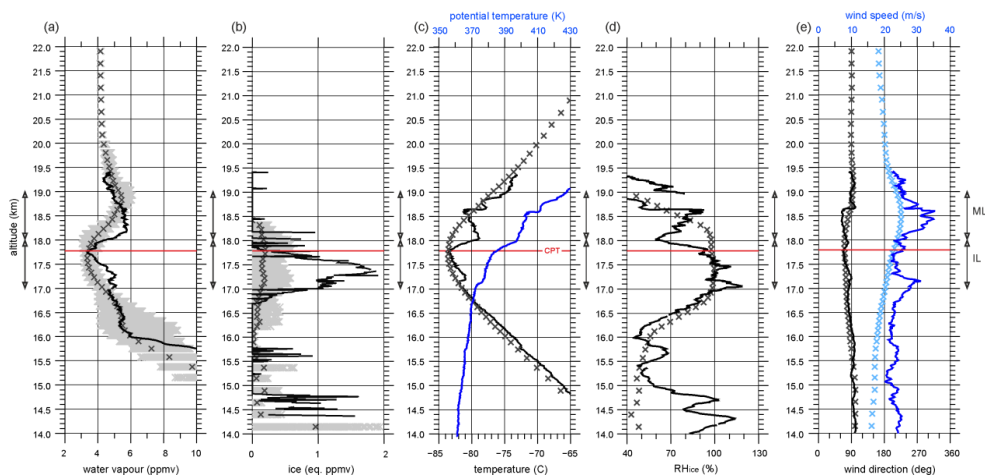
567



568

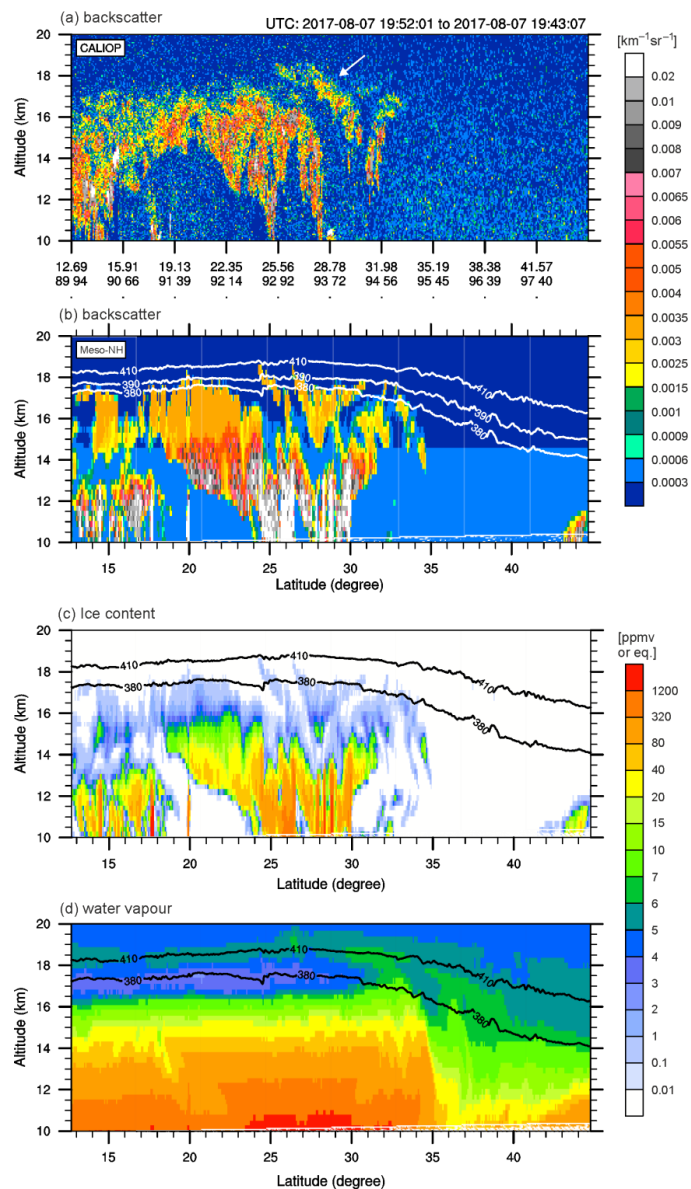
569 **Figure 1.** Topography and domain considered in the Meso-NH numerical simulation with a resolution of 2.5 km. The trajectory of the
570 Geophysica flight #7 to the south of Kathmandu is shown by the red solid line, while the pathway of moist patch (25–26.5°N) is
571 depicted by the blue line. A black box ‘HYD’ is a model domain considered in comparison with aircraft measurement. Another box
572 with dashed line is a model domain used to calculate the background water vapour at 06:00 UTC on 8 August 2017. The track of
573 CALIOP around 20:00 UTC on 7 August 2017 is shown by the black solid line while its track between 25 and 33°N is highlighted in
574 yellow.

575



576

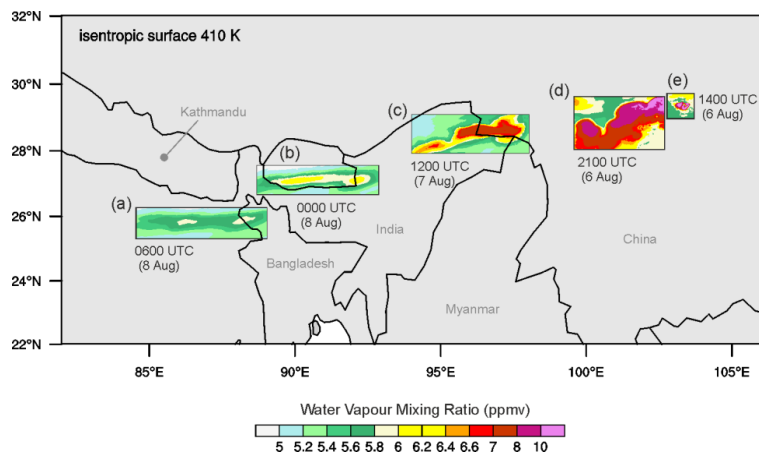
577 **Figure 2.** Vertical profiles of (a) water vapour (ppmv), (b) ice (eq. ppmv), (c) temperature ($^{\circ}\text{C}$) and potential temperature (K), (d)
578 relative humidity respect to ice (RH_{ice} , %), and (e) wind direction (degree) and speed (m s^{-1}). In (a)–(e), the measured values along the
579 blue-coloured track between $25\text{--}26.5^{\circ}\text{N}$ (shown in Fig. 1) from 06:20 to 06:48 UTC on 8 August 2017 are shown as solid line, while
580 the domain averaged values in the region ‘HYD’ ($25\text{--}26.5^{\circ}\text{N}$, $85\text{--}85.5^{\circ}\text{E}$, shown in Fig. 1) from the Meso-NH simulation at 06:00
581 UTC on the same day are shown as cross marks. In (a)–(e), the level of cold point tropopause (CPT) is indicated by a red line. In
582 (a)–(b), all the values from Meso-NH within the ‘HYD’ is displayed by grey cross marks. The layers of ML and IL are marked by
583 arrows.



584

585 **Figure 3.** Backscatters at 532 nm (a) measured by CALIOP around 20:00 UTC and (b) retrieved by the Meso-NH simulation, and ice
586 content (eq. ppmv) and water vapour (ppmv) produced by the Meso-NH simulation along the CALIOP track (marked by solid line in
587 Fig. 1) at 20:00 UTC on 7 August 2017.

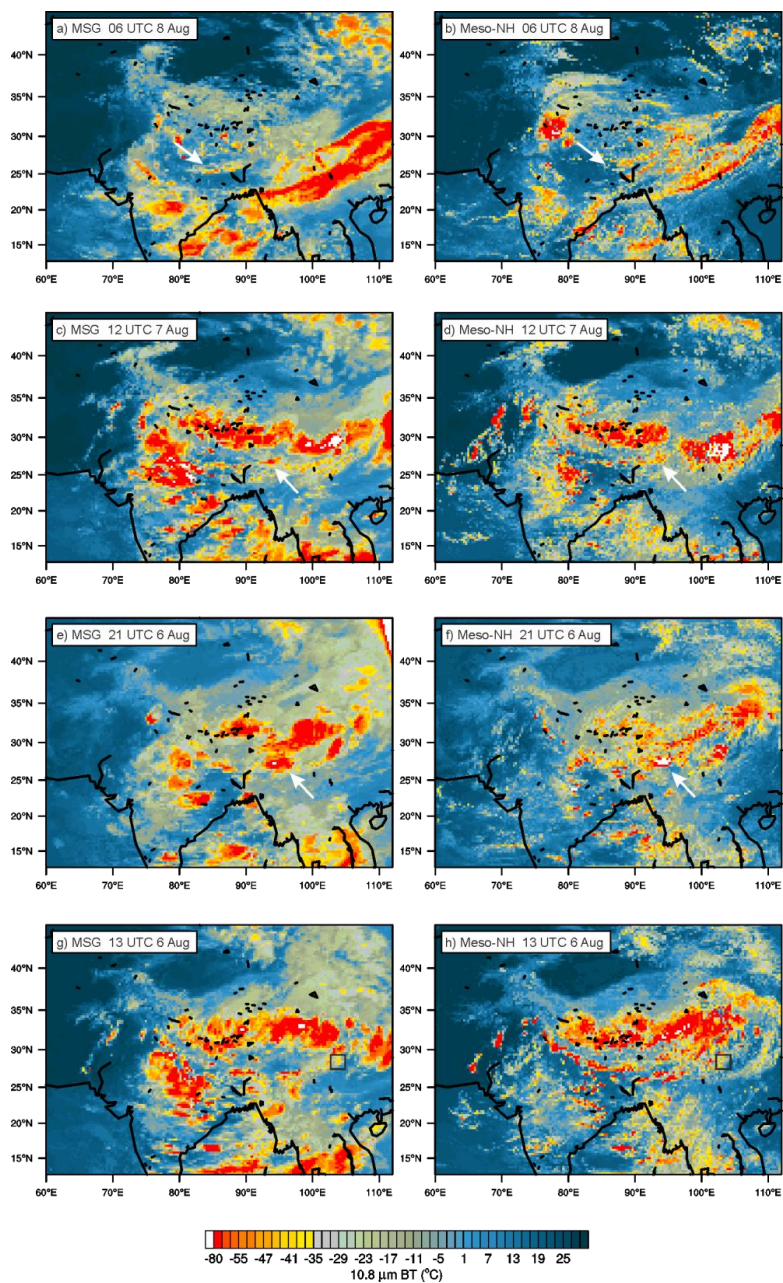
588



589

590 **Figure 4.** Target moist patch. Horizontal distribution of water vapour mixing ratio at 410 K isentropic altitude at (a) 06:00 UTC, and

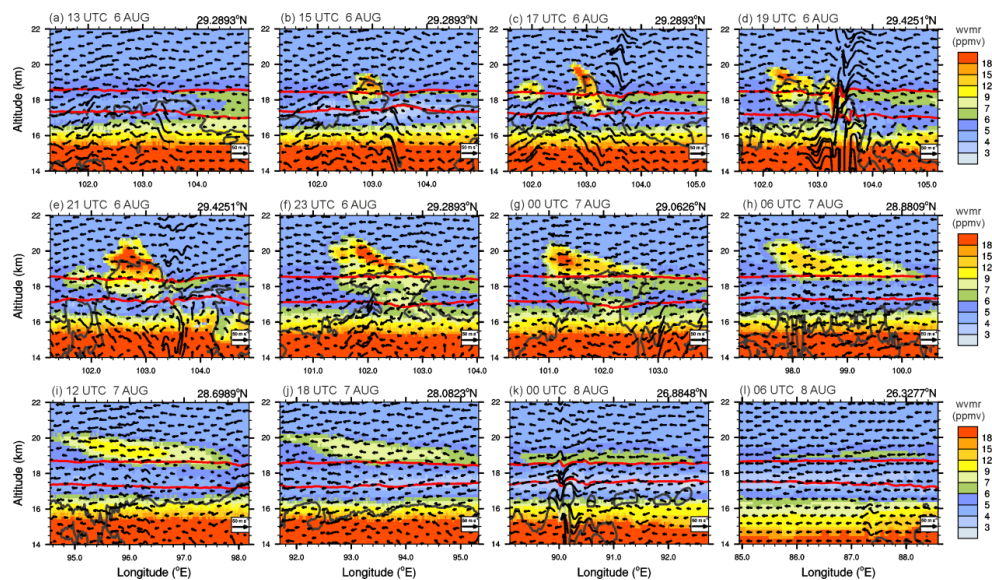
591 (b) 00:00 UTC on 8 August, (c) 12:00 UTC on 7 August, (d) 21:00 UTC and (e) 14:00 UTC on 6 August 2017.



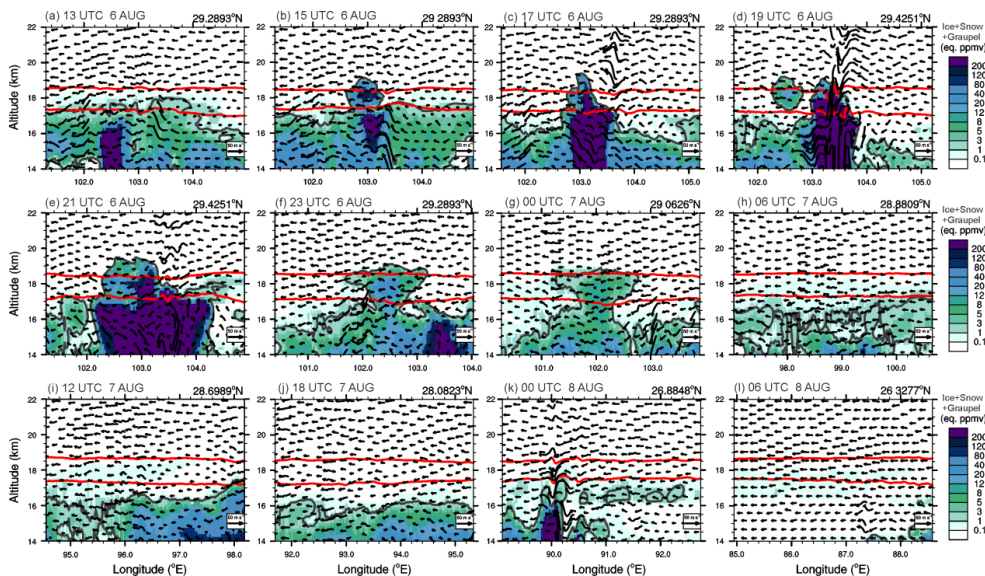
592

593 **Figure 5.** BT 10.8 μm obtained from SEVIRI/MSG (left) and Meso-NH (right) at (a)–(b) 06:00 UTC on 8 August, (c)–(d) 12:00 UTC

594 on 7 August, (e)–(f) 21:00 UTC, and (g)–(h) 13:00 UTC on 6 August 2017.



595
596 **Figure 6.** Vertical cross-sections of water vapour mixing ratio (a) 13:00 UTC, (b) 15:00 UTC, (c) 17:00 UTC, (d) 19:00 UTC, (e)
597 21:00 UTC, (f) 23:00 UTC on 6 August 2017, (g) 00:00 UTC, (h) 06:00 UTC, (i) 12:00 UTC, (j) 18:00 UTC on 7 August 2017,
598 and (k) 00:00 UTC and (l) 06:00 UTC on 8 August 2017. The isentropic altitudes of 380 and 410 K are depicted by the red lines. The
599 latitude (°N) of west-east oriented cross-section line is indicated at the upper right of each panel. The cloud boundary (mixing ratio of
600 ice content of 10 mg kg^{-1}) is contoured by the black solid line.
601



602

603

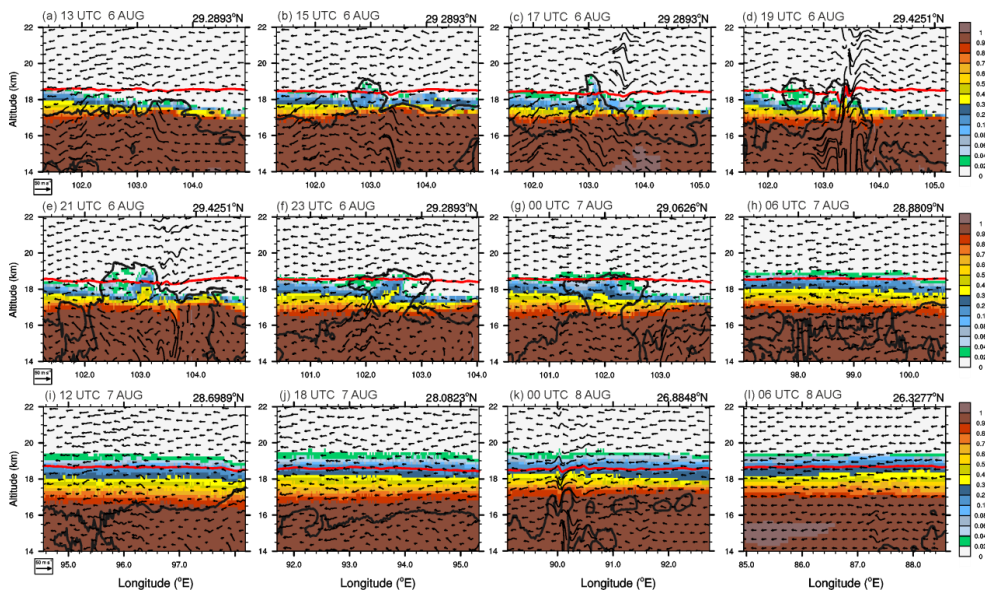
604

605

606

607

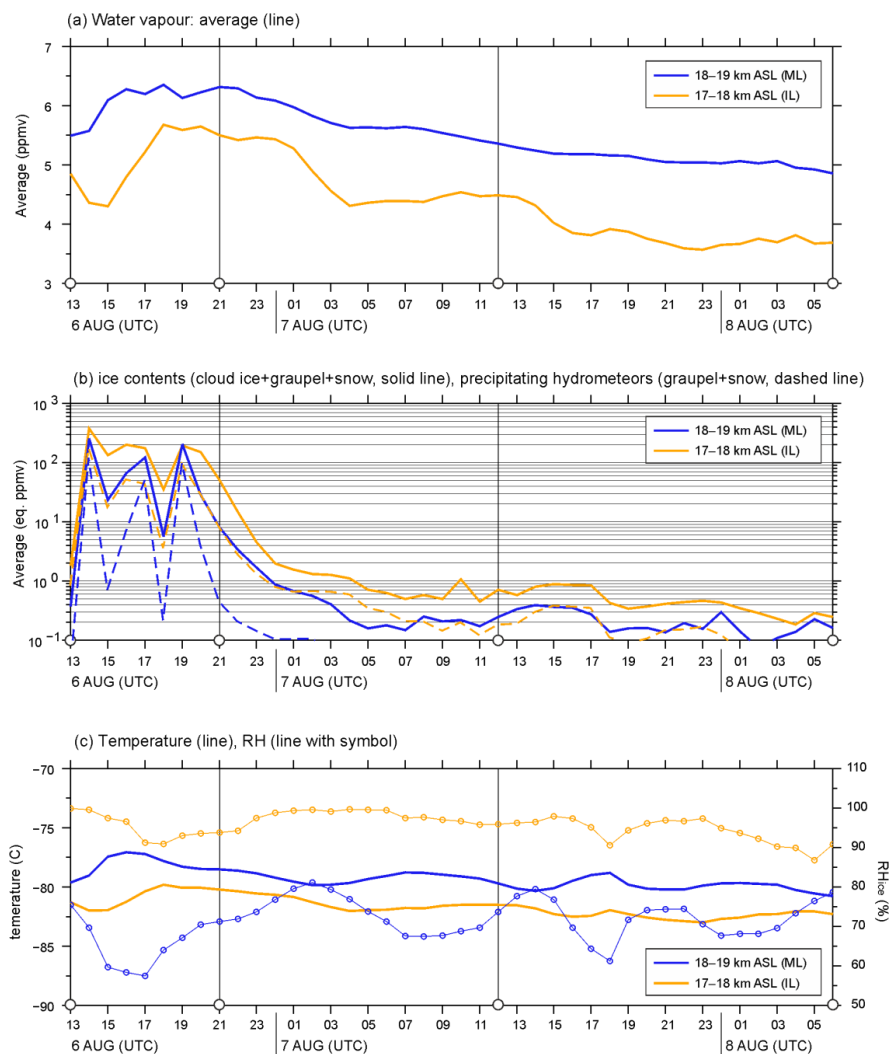
Figure 7. Same as Fig. 6 but for the ice content. The isentropic altitudes of 380 and 410 K are depicted by the red lines.



608

609

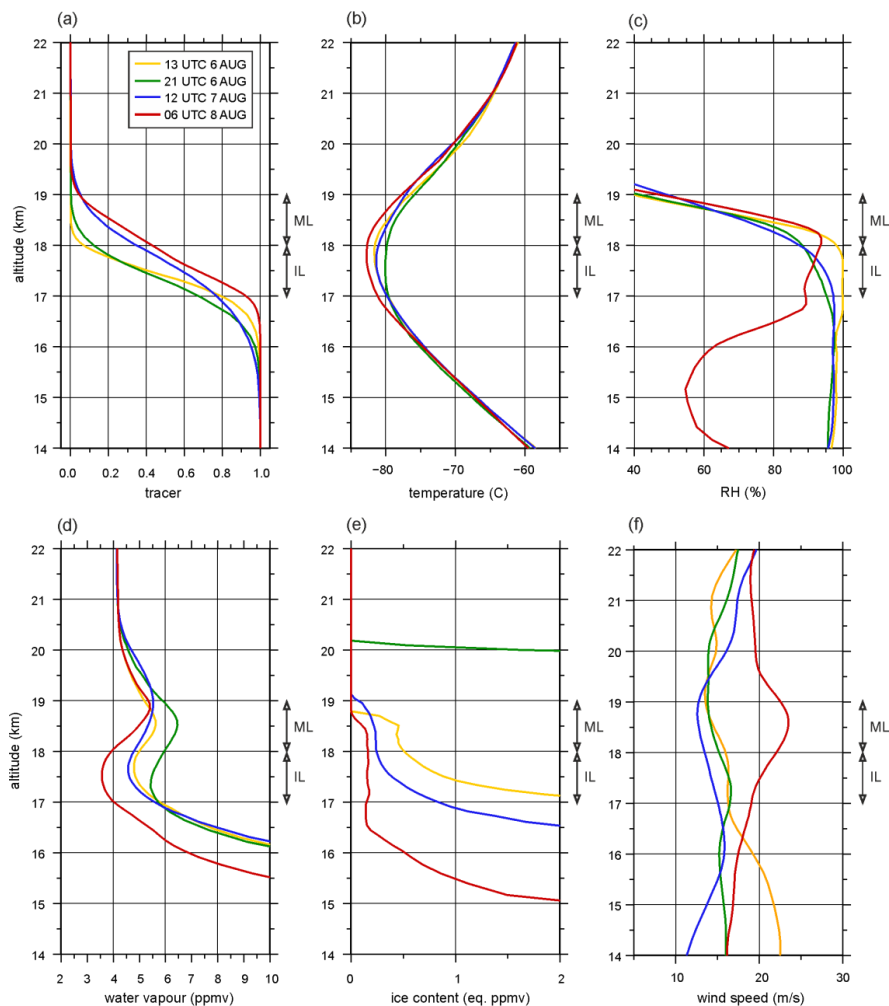
Figure 8. Same as Fig. 6 but for the tracer. The isentropic altitude of 410 K is depicted by the red line.



610

611 **Figure 9.** Hourly evolution of (a) averaged water vapour (line), (b) averaged ice content (solid line, sum of ice, graupel, and snow) and
612 the precipitating hydrometeor (dashed line, sum of graupel and snow), and (c) averaged temperature (line) and relative humidity (RH_{ice},
613 thin line with circle) in the altitudes of 17–18 km (yellow lines) and 18–19 km (blue lines) ASL from 13:00 UTC on 6 August to 06:00
614 UTC on 8 August 2017. The four analysis times are marked by open circles on the x-axis. Average and maximum values are calculated
615 in ML and IL.

616

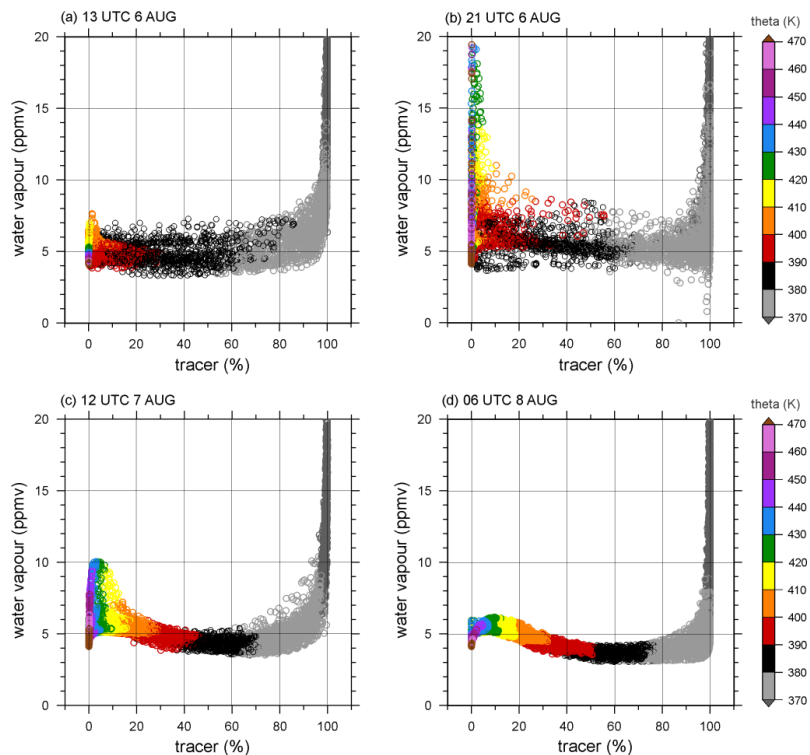


617

618 **Figure 10.** Vertical profiles of (a) tracer, (b) temperature (°C), (c) relative humidity (%), mixing ratios of (d) water vapour (ppmv), (e)619 ice content (eq. ppmv), and (f) wind speed (m s^{-1}) across the hydration patch along the trajectory at 13:00 UTC (yellow line), 21:00

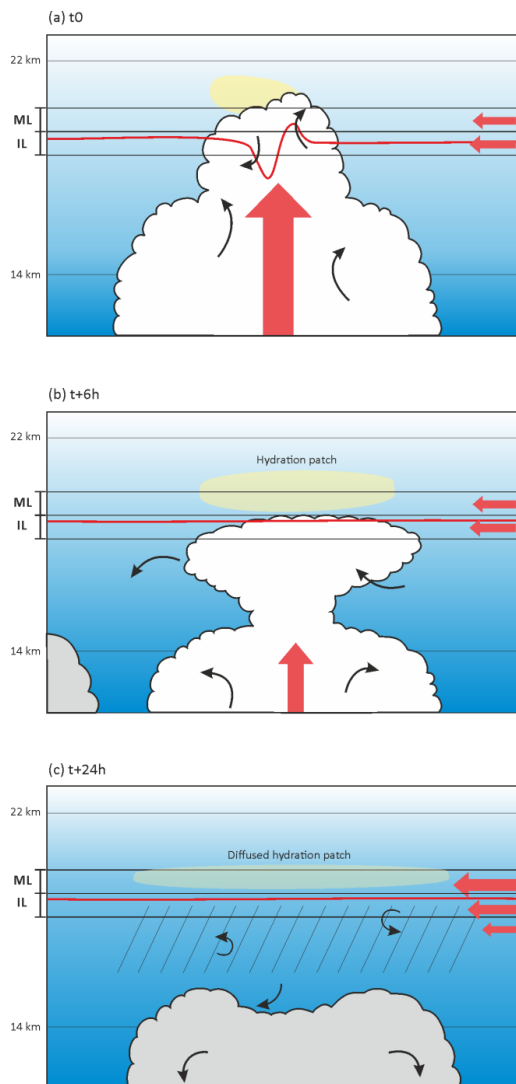
620 UTC (green line) on 6 August, 12:00 UTC on 7 August (blue line), and 06:00 UTC (red line) on 8 August 2017. The layers of ML and

621 IL are marked by arrows.



622

623 **Figure 11.** Mixing diagram using tropospheric tracer (%) and water vapour (ppmv) across the hydration patch in the altitudes between
624 14 and 22 km ASL along the trajectory at (a) 13:00 UTC on 6 August, (b) 21:00 UTC on 6 August, (c) 12:00 UTC on 7 August, and
625 (d) 06:00 UTC on 8 August 2017. The potential temperature (K) is shown with colour shading.



626

627 **Figure 12.** Schematic illustration summarising the hydration process in the TTL during flight #7 of the StratoClim 2017 field campaign.

628 (a) Mixing of the overshoots with the stratospheric air, (b) and (c) turbulent mixing of the hydration patch with the tropospheric air by
629 vertical wind shear. The bottom and top of the TTL, 14 and 22 km, and the moist layer (ML) and ice layer (IL) are represented by the
630 black solid line, and the 410 K isentropic altitude is represented by the red solid line. The main force in the TTL is marked by bold red
631 arrows, while the turbulent eddies in/around the developed and weakened overshoots are described by black arrows. The overreaching
632 water vapour above the cloud top level is indicated by a yellow ellipsoid in (a). The hydration patch is yellow-encapsulated in (a) and
633 (b), and the layer of sublimating ice content is hatched in (c). The blue shades illustrate the concentration of tropospheric air, showing
634 the increased tropospheric air in the TTL by the turbulent mixing in (b) and (c).